Design and Finite Element Analysis of a Novel Permanent Magnet Assisted Reluctance Synchronous Motor

Xianming Deng, Ran Li, Lei Hao, Ankang Zhang, and Junhong Zhou

Jiangsu Province Laboratory of Mining Electric and Automation, China University of Mining and Technology
Xuzhou, 221116, China
xmdengcumt@126.com, marchliran@163.com

Abstract ─ In this paper, a permanent magnet assisted synchronous reluctance machine (PMASRM) with optimized permanent magnet width and asymmetric rotor structure is proposed. A typical PMASRM is selected as the reference motor (Pre-optimized PMASRM). In order to reduce the large torque ripple of conventional PMASRM, an optimization method to design the permanent magnet width is investigated and the Optimized Magnet-width PMASRM is proposed. On this basis, an asymmetric flux barriers structure is proposed to further reduce the torque ripple. Some electromagnetic characteristics including air-gap flux density, no-load back EMF and motor efficiency are examined by Finite Element Analysis (FEA). The simulation results show that the proposed PMASRM can not only decrease the harmonic component of no-load back EMF obviously, but also reduce the torque ripple in steady-state operation, which proves the rationality of the motor structure.

Index Terms ─ Asymmetric flux barriers, Finite Element Analysis (FEA), magnet width, PMASRM, torque ripple.

I. INTRODUCTION

The typical structure of PMASRM is to put the permanent magnet in the proper position of the flux barrier in the synchronous reluctance machine (SRM). In order to obtain higher torque density and improve power factor, the ferrite permanent magnet material which is slightly weaker than rare earth permanent magnet but more widely sourced and cheaper is usually used [1]. So ferrite PMASRM is widely used in industry because of its high cost performance, good thermal stability, wide speed range and no over voltage risk. Measures to achieve high torque density, low torque ripple, high power factor, low iron loss and high mechanical strength were summarized [2], and the problem of demagnetization of ferrite is also discussed [3]. A PMASRM by using one step or more than two axially laminate rotors with asymmetric flux-barrier is proposed which can reduce the torque ripple but not to decrease the average torque [4]. Methods to improve torque ripples and cogging torque of SRM are investigated and proposed [5]. Flux barriers are asymmetrically designed so that the relative position relation between outer edge of flux barriers and teeth may not be in agreement, which reduces torque ripple dramatically [6]. In addition, two ferrite PMASRM using asymmetric rotor structure with shifted flux barriers and enlarged opening angle of flux barrier respectively are also proposed to improve the motor performance, which have a greater improvement in efficiency and torque ripple [7, 8].

Torque of PMASRM is consisted by two parts: basic torque by the interaction between the rotor permanent magnet field and the stator magnetic field, which is called the permanent magnet torque; as well as the second one donating reluctance torque caused by the unequal reluctance of d-axis and q-axis [9]. When reluctance torque plays a greater role than permanent magnet torque, the motor exhibits higher salient polarity. In order to obtain higher saliency, PMASRM is usually designed as a multi-layer flux barrier structure. Nowadays, the widely used PMASRM structures include "U" type flux barrier, arc type flux barrier, V type flux barrier and hybrid type flux barrier [10-13] as shown in Fig. 1.

The most important disadvantage of PMASRM is that the inherent torque ripple is large and the harmonic content of no-load back EMF is not easy to filter [14]. Aiming at these shortcomings of PMASRM, a novel design method of PMASRM is proposed in this paper. Firstly, a PMASRM with "U" type magnetic barrier is selected as the Pre-optimized PMASRM and its shortcomings are analyzed by finite element simulation. Then, without changing the size of the motor and the consumption of permanent magnets, two optimization schemes are proposed and simulated by FEA. Finally, this paper compares the two optimized motors with the Pre-optimized PMASRM. The simulation results show that the performance of the optimized motor is better than that of the former motor, which proves the rationality of the design.

Submitted On: June 22, 2019
Accepted On: June 29, 2020

https://doi.org/10.47037/2020.ACES.J.350906

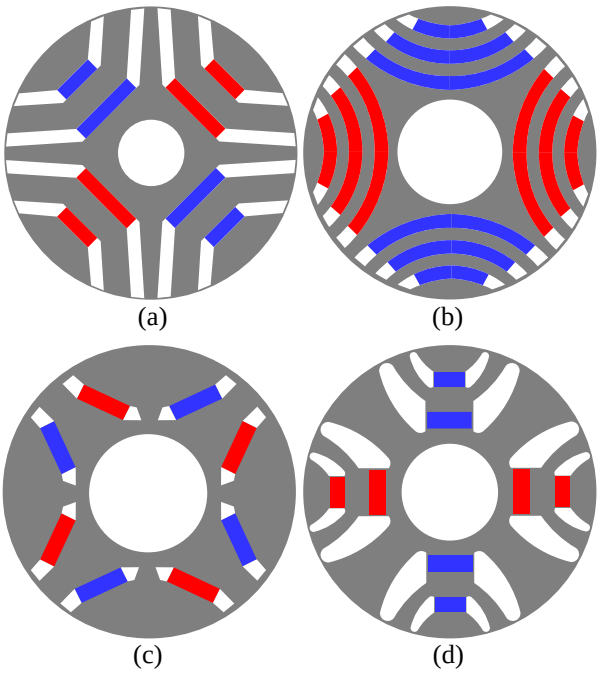

Fig. 1. (a) 'U' type flux barrier, (b) arc type flux barrier, (c) 'V' type flux barrier, and (d) hybrid type flux barrier.

II. PRINCIPLE AND CHARACTERISTIC ANALYSIS OF PRE-OPTIMIZED PMASRM

A. Basic parameters design of motor

Basic parameters include the main size of motor, the size and working point of permanent magnet, slot and stator winding. If the slot type is not suitable or load is not satisfied, it is necessary to adjust the size of permanent magnet and its correspondence parameters to meet design requirements and technical and economic indicators.

Table 1: Main parameters of the motor

Parameters	Value
Rated power/W	550
Rated speed/rpm	1000
Rated line voltage/V	380
Frequency/Hz	50
Stator outer diameter/mm	62.5
Stator inner diameter/mm	38.75
Core length/mm	85
Number of poles	6
Stator slot number	36
Height of magnet/mm	2
Ferrite magnet type	FB9B
Steel type	D2350

The main dimensions of the motor are the inner and outer diameters of stator and rotor, the length of stator core and the effective length of air-gap, etc. The main dimensional relationship of the induction motor can be approximated by using to derive the main size relations of the motor. Selected main parameters of motors are shown in Table 1 below.

The decision to select FB9B as the ferrite permanent magnet material is based on its basic performance, which is better than several similar permanent magnets.

B. Design of rotor structure

Considering the processing cost affected by the shape of the rotor and the permanent magnet, the 'U' type flux barrier structure is adopted for the rotor of the Pre-optimized PMASRM. Furthermore, the maximum output torque of one-layer, two-layer and three-layer flux barrier structures increases obviously as the number of layer increases. However, the maximum output torque of four-layer flux barrier structure and five-layer flux barrier structure does not increase significantly compared with three-layer flux barrier structure, on the contrary, that will increase its torque ripple [15]. Considering the above facts comprehensively, this paper chooses three-layer 'U' flux barrier structure rotor as the Pre-optimized PMASRM rotor, and chooses three-layer permanent magnets in equal width and height to insert into the flux barriers. The section diagram of the Pre-optimized PMASRM is shown in Fig. 2.

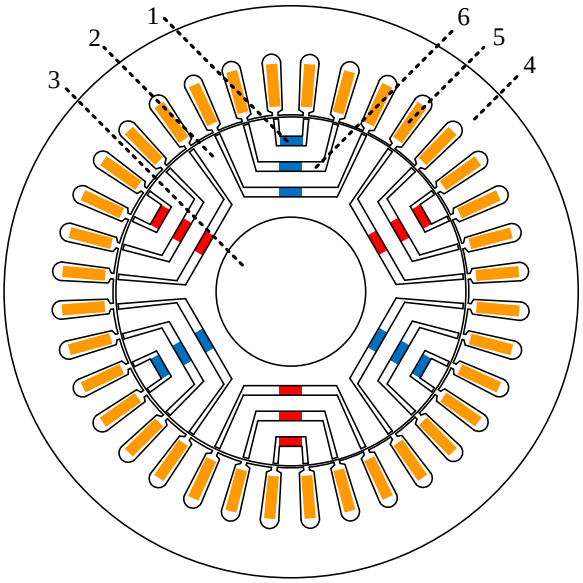

1-Permanent magnet, 2-Rotor core, 3-Shaft,
4-Stator core, 5-Stator winding, 6-Flux barrier

Fig. 2. FEA model of the pre-optimized PMASRM.

C. FEA of pre-optimized PMASRM

In this paper, Maxwell FEA software is used to establish the model of the Pre-optimized PMASRM and the FEA is carried out. The air-gap flux density curve, no-load back EMF waveform, power angle

characteristics and rated load operation performance of the Pre-optimized PMASRM are obtained and its shortcomings are analyzed.

FEA was used to analyze the Pre-optimized PMASRM. The air-gap flux density and no-load back EMF were solved by Ansoft field calculator. Fourier analysis and harmonic content comparison of air-gap flux density waveform and no-load back EMF waveform were carried out and the THD of no-load back EMF waveform was calculated.

From Fig. 3 (b) and Fig. 4 (b), the harmonic component of the air-gap flux density waveform of the Pre-optimized PMASRM is large. Similarly, the harmonic component of the no-load back EMF is also large, especially the third harmonic component accounts for a large proportion. The THD is 48.38%.

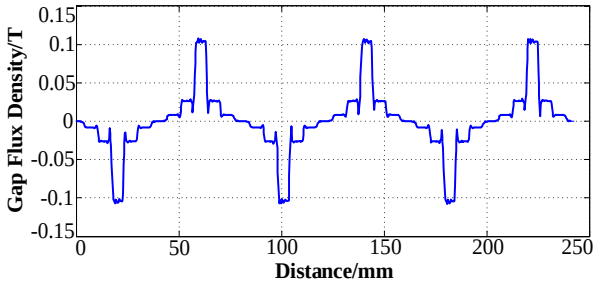

(a)

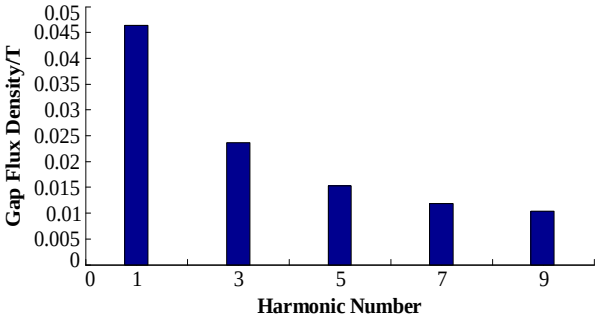

(b)

Fig. 3. (a) Air-gap flux density waveform of the pre-optimized PMASRM, and (b) harmonic analysis results of air-gap flux density for pre-optimized PMASRM.

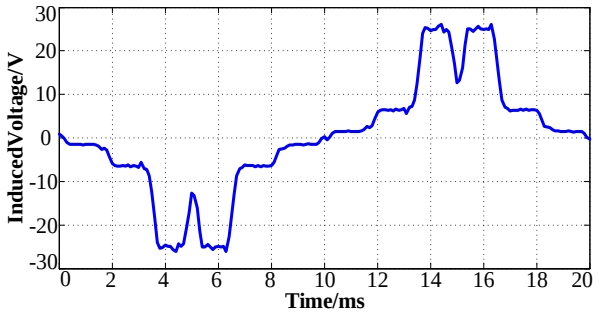

(a)

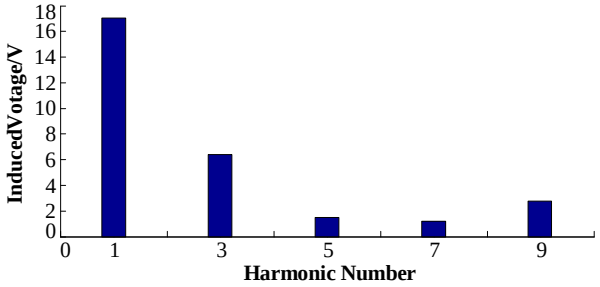

(b)

Fig. 4. (a) No-load back EMF waveform of the pre-optimized PMASRM, and (b) harmonic analysis results of no-load back EMF for the pre-optimized PMASRM.

D. Analysis of power angle characteristics

In order to obtain the power angle characteristics of Pre-optimized PMASRM, it is necessary to calculate the torque. By setting different power angles in Maxwell software and calculating the corresponding torque values of different power angles through FEA, the power angle characteristics of permanent magnet synchronous motor are obtained. Usually, the resistance of stator winding is small, so its influence is neglected. The torque of PMASRM is given by [16]:

$$T_{em}=m\frac{E_0U}{X_d\Omega_s}\sin\delta+m\frac{U^2}{2\Omega_s}\left(\frac{1}{X_q}-\frac{1}{X_d}\right)\sin 2\delta, \quad (1)$$

where m is phase number, E_0 is no-load EMF, U is power supply voltage, Ω_s is mechanical angular velocity, δ is power angle, X_d and X_q are d-axis and q-axis reactance, respectively.

It can be seen from (1) that the torque consists of two parts: basic torque by the interaction between the rotor permanent magnet field and the stator magnetic field, which is called the permanent magnet torque; as well as the second one donating reluctance torque caused by the unequal reluctance of d-axis and q-axis. Figure 5 is the torque component diagram of the ferrite PMASRM. The main component of torque is reluctance torque, so the maximum output torque occurs when the power angle is greater than 90 degrees, while in a certain range before 90 degrees, the torque is negative [17]. Figure 6 is the power angle characteristics of Pre-optimized PMASRM.

III. ELECTROMAGNETIC DESIGN OF OPTIMIZED MAGNET-WIDTH PMASRM

In order to solve the problems of large harmonic component of air-gap flux density waveform and THD of no-load back EMF of Pre-optimized PMASRM, a novel motor structure designed by optimizing the width of multi-layer permanent magnet is proposed, which is called Optimized Magnet-width PMASRM in the following. It makes the harmonic component of air-gap

flux density waveform and no-load back EMF waveform less, so that the waveforms are closer to sinusoidal wave.

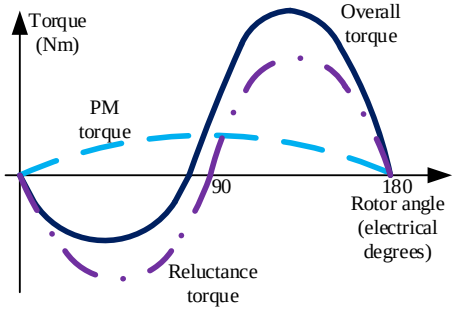

Fig. 5. Torque component of the ferrite PMASRM.

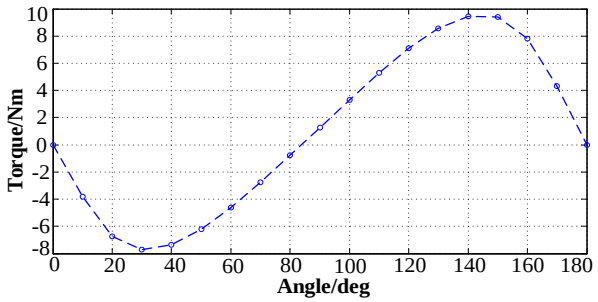

Fig. 6. Power angle characteristics of pre-optimized PMASRM.

A. Calculation of magnetic circuit

Ignoring the stator core magnetoresistance and the rotor core magnetoresistance, an equivalent magnetic circuit diagram of the magnetic circuit for Pre-optimized PMASRM can be obtained [18], as shown in Fig. 7.

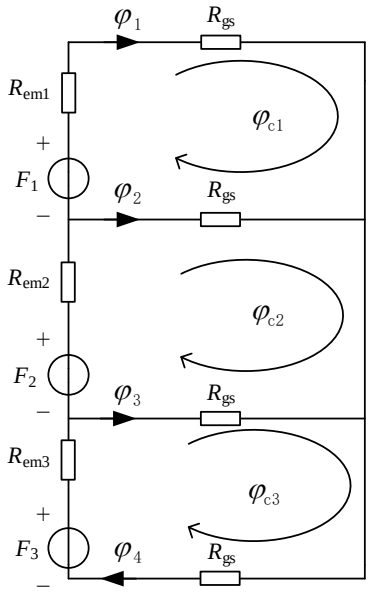

Fig. 7. Equivalent magnetic circuit.

In Fig. 7 F_1, F_2 and F_3 are magnetic motive force of PM1, PM2 and PM3, respectively; R_{em1}, R_{em2} and R_{em3} are reluctance of PM1, PM2 and PM3, respectively; R_{gs} is the reluctance of air-gap; $\phi_1, \phi_2, \phi_3, \phi_4$ are branch flux; $\phi_{c1}, \phi_{c2}, \phi_{c3}$ are loop flux.

From Fig. 7, because the thickness of the permanent magnet is much larger than the air-gap width of the motor and the thickness of three layers of permanent magnets is equal, this paper assumes that:

$$R_{em1} = R_{em2} = R_{em3} = \alpha R_{gs}. \tag{2}$$

In (2), α>1.

Similar to the principle of superposition in electric circuits, the principle of superposition can also be used in magnetic circuits. For a linear system, the response of any branch of a bilateral linear magnetic circuit with multiple independent sources equals the algebraic sum of the response of each independent source acting alone, at which time all other independent sources are replaced by their respective impedance. Because the ferrite permanent magnet is chosen, the core is far from saturated, so it can be approximated as a linear system. When only one magnetic motive force of F_1 acts on the whole magnetic circuit, the equivalent magnetic circuit can be obtained as follows.

In Fig. 8,

$$\begin{aligned} R_* &= \frac{(R_{em3}+R_{gs})R_{gs}}{R_{em3}+2R_{gs}} + R_{em2} \\ &= \alpha + (\frac{1+\alpha}{2+\alpha})R_{gs} \gg R_{gs} \end{aligned}. \tag{3}$$

A and B are inversely proportional to the reluctance of their magnetic branches, so,

$$\frac{\varphi_1}{\varphi_{*1}} = \frac{R_*}{R_{gs}} = \frac{\alpha + (\frac{1+\alpha}{2+\alpha})R_{gs}}{R_{gs}} = \alpha + \frac{1+\alpha}{2+\alpha}. \tag{4}$$

Therefore, φ_1>>φ_{*1}, the flux lines stimulated by F_1 mostly pass through φ_1 to form a loop, and the very small part of them pass through φ_{*1} to form a loop. So, φ_1 can be regarded as all the flux lines stimulated by F_1. Similarly, φ_2 and φ_3 can be seen as all the flux lines stimulated by F_2 and F_3, respectively.

From Fig. 3 (a), the air-gap flux density waveform of the Pre-optimized PMASRM waveform is closer to the rectangular waveform because the magnetic lines passing through L_2 and L_3 are almost zero. Because $\varphi_{l1} \approx \varphi_{l2}$, so,

$$\varphi_2 = \varphi_{l2} - \varphi_{l1} \approx 0. \tag{5}$$

Similarly,

$$\varphi_3 = \varphi_{l3} - \varphi_{l2} \approx 0. \tag{6}$$

If the waveform of air-gap flux density is expected to be closer to sinusoidal waveform, then it is necessary to make φ_2>0. On the premise of keeping the motor size and rotor core unchanged, that is, R_{gs} and R_{emi} (i = 1, 2,

3) unchanged, only F_2 can be increased to make $F_2 > F_1$; similarly, F_3 should be increased to make $F_3 > F_2$. So in total: $F_3 > F_2 > F_1$.

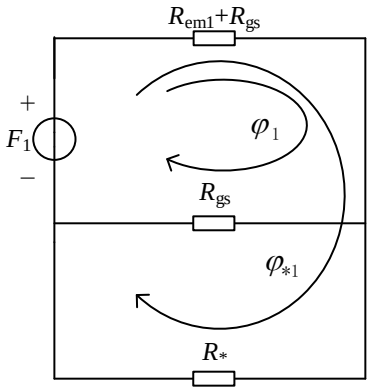

Fig. 8. Equivalent magnetic circuit with F_1 working alone.

B. Optimization strategy of optimized magnet-width PMASRM

According to the special multi-layer flux barrier structure of PMASRM, the outer surface of the rotor can be divided into several parts. As shown in Fig. 9, taking the three-layer flux barrier structure as an example, the outer surface of the rotor can be divided into four parts, namely L_1, L_2, L_3 and L_4.

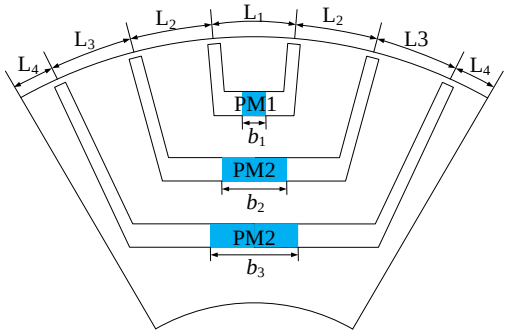

Fig. 9. The rotor model for single pole.

The flux path of motor without load is observed by FEA. In Fig. 10, distribution of flux lines under no-load is shown and three representative routes of magnetic lines are marked. It is found that the flux line which goes through L_3 is generated by PM3; which goes through L_2 is generated by PM2 and PM3; which goes through L_1 is generated by PM1, PM2 and PM3. Therefore, the amount of magnetic lines going through L_1, L_2, L_3 and L_4 can be adjusted by properly distributing the volumes of PM1, PM2 and PM3, so that the waveform of air-gap flux density is closer to sinusoidal wave.

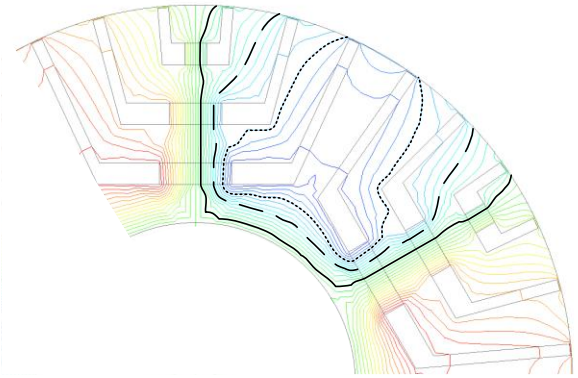

Fig. 10. Distribution of flux lines of two poles under no-load.

This paper assumes that the magnetic line φ_3 passing through L_3 is generated by more parts of PM3 than PM2. Similarly, the magnetic line φ_2 passing through L_2 is generated by more parts of PM2 than PM1. α_1, α_2, α_3 and α_4 are the angles crossed by L_1, L_2, L_3 and L_4, respectively. Therefore, after the rotor flux barrier structure is determined, which means after the determination of α_1, α_2, α_3 and α_4, there is an optimal distribution of the width of PM1, PM2 and PM3, which makes the harmonic component of the air-gap flux density waveform smaller under no-load condition. Figure 11 shows the distribution of air-gap flux density curve under one magnetic pole. B_{g3} is produced by PM3, B_{g2} is produced by PM3 and PM2 together, B_{g1} is produced by PM1, PM2 and PM3.

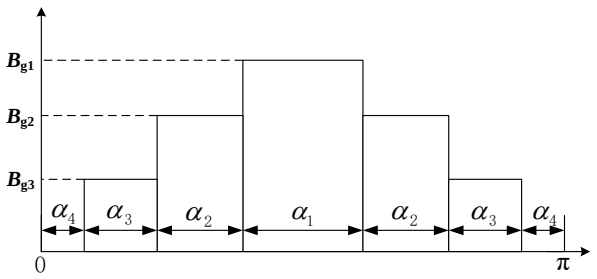

Fig. 11. Distribution of air-gap flux density of single pole under no-load condition.

C. Calculation of the width of permanent magnet basic

As it can be seen in Fig. 10, **the magnetic flux density** generated by the permanent magnet is proportional to the width of the permanent magnet. Under the premise that the angle of the flux barrier of the motor remains unchanged, the area equivalent principle (that is, the area of the corresponding part of the air-gap flux density waveform is proportional to the width of the permanent magnet) is used to calculate.

Comprehensively considering the manufacturing cost of rotor punching and permanent magnets, the magnetic barrier height of each layer is h=2mm, the rotor core length is l=85mm, and the amount of permanent magnets per pole is V=7584mm^3. According to the model in Fig. 2, the angle α_1=10° crossed by the first layer of magnetic barrier corresponds to the electrical angle $\beta_1=p\alpha_1$=30° (p is the number of pole pairs). Similarly, the electrical angles crossed by the second and third layers of magnetic barrier are B_2 = 90° and β_3 = 150°, respectively. In Fig. 11, the area of the ideal sinusoidal flux waveform corresponding to the electrical angle crossed by the first layer of magnetic barrier is:

$$S_1=\int_{90°-\frac{\beta_1}{2}}^{90°+\frac{\beta_1}{2}}\sin x\mathrm{d}x=0.518. \tag{7}$$

Similarly, the area corresponding to the second and third layer of magnetic barrier are:

$$S_2=\int_{90°-\frac{\beta_2}{2}}^{90°+\frac{\beta_2}{2}}\sin x\mathrm{d}x=1.415, \tag{8}$$

$$S_3=\int_{90°-\frac{\beta_3}{2}}^{90°+\frac{\beta_3}{2}}\sin x\mathrm{d}x=1.933. \tag{9}$$

Therefore, the width of the permanent magnet in the first layer of magnetic barrier is calculated by:

$$b_1=\frac{V}{3hl}\frac{S_1}{\sum_{i=1}^{3}S_i}=2\text{mm}. \tag{10}$$

Similarly, the widths of the second and third layer of magnetic barrier permanent magnets b_2 and b_3 are 5.4mm and 7.4mm, respectively. The structure of the Optimized Magnet-width PMASRM is shown in Fig. 12.

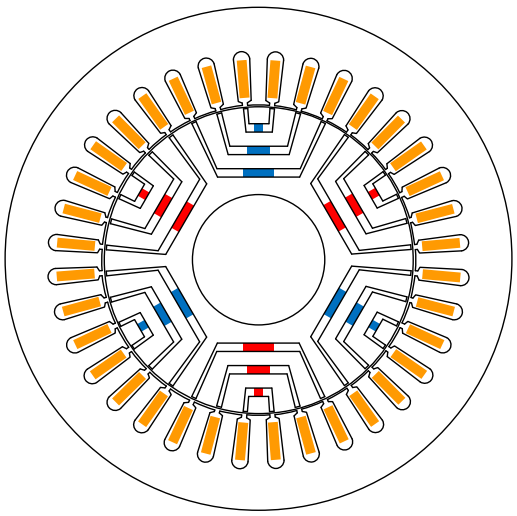

Fig. 12. FEA model of the optimized magnet-width PMASRM.

D. FEA of the optimized magnet-width PMASRM

Similar to the Pre-optimized PMASRM, the FEA of the Optimized Magnet-width PMASRM was carried out by Maxwell software. The air-gap flux density waveform and the harmonic content of Fourier analysis, no-load back EMF waveform, harmonic content, distortion rate and torque ripple under rated conditions were analyzed.

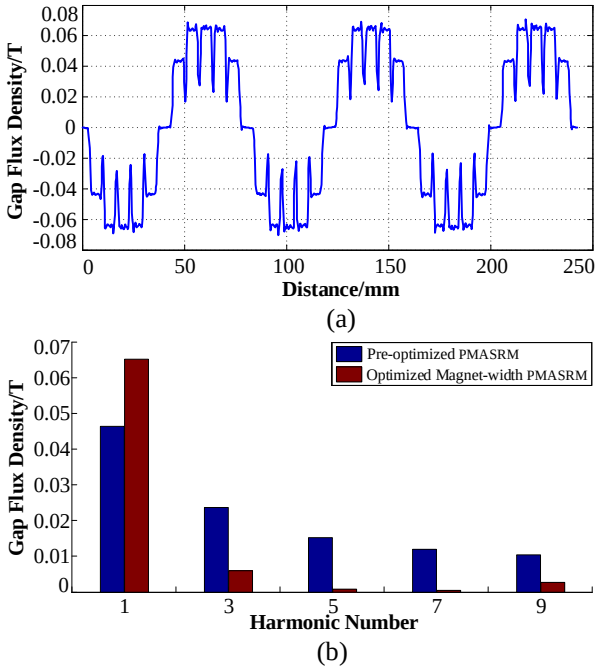

Fig. 13. (a) Air-gap flux density waveform of optimized magnet-width PMASRM, and (b) hanalysis results of no-load back EMF for two kinds of motors.

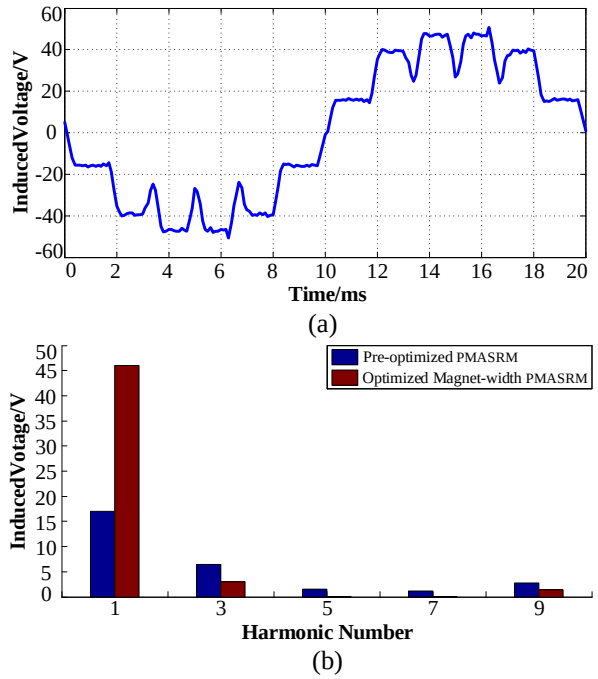

Fig. 14. (a) No-load back EMF waveform of optimized magnet-width PMASRM, and (b) harmonic analysis results of no-load back EMF for two kinds of motors.

By comparing and analyzing the harmonics of air-gap flux density harmonics in Fig. 13 and no-load back EMF harmonics of Optimized Magnet-width PMASRM in Fig. 14, the no-load back EMF and the fundamental wave content of air-gap flux density of Optimized Magnet-width PMASRM increase significantly compared with the Pre-optimized PMASRM. Besides, the fifth, seventh and ninth harmonics have been reduced. Moreover, THD of no-load back EMF is reduced from 48.38% to 18.52%. Therefore, the Optimized Magnet-width PMASRM reduces the harmonic component, making the induction EMF waveform and air-gap flux density waveform closer to sinusoidal waveform.

This paper uses Maxwell software and FEA. The three-phase symmetrical rated voltage is applied to the three-phase stator windings of the Pre-optimized PMASRM and the motor with Pre-optimized PMASRM. Both motors have rated loads. The current distortion and torque ripple of the two motor structures under rated loads are observed in Fig. 15 (in this paper, the torque ripple is defined as peak to peak torque values).

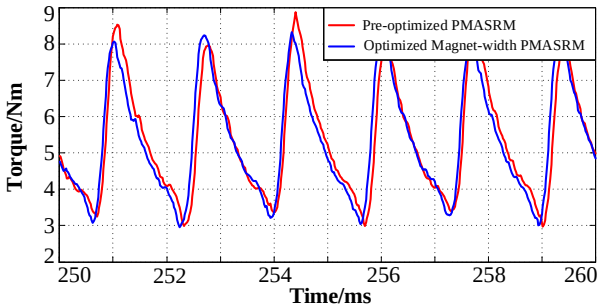

Fig. 15. Torque ripple for two kinds of motors.

The simulation results show that, with the same load, compared with the Pre-optimized PMASRM, the torque ripple of Pre-optimized PMASRM decreases from 5.89Nm to 5.51Nm. Because these two structures have same core structure of the motor, that is to say, the torque ripple caused by reluctance torque is not weakened. The weakening part of the torque ripple is due to the optimization of permanent magnet torque. Because the reluctance torque accounts for a large proportion in the ferrite motor, it is necessary to optimize the structure of the rotor core in order to optimize the torque ripple to a large extent. Considering that the torque ripple of the Pre-optimized PMASRM is still slightly larger, in the following sections, an optimization scheme of asymmetric flux barrier rotor structure is proposed to further weaken the torque ripple.

IV. ELECTROMAGNETIC DESIGN OF ASYMMETRIC FLUX BARRIER PMASRM

In order to further weaken the torque ripple and minimize the harmonic distortion rate of no-load back EMF on the basis of Pre-optimized PMASRM, the design optimization of the rotor core are investigated.

Because the PMASRM exhibits high anisotropy, the salient polarity of the rotor leads to serious torque ripple. Generally, there are two sources of torque ripple in PMASRM: one is the interaction between stator and rotor magnet motive potentials, the other is the uneven change of reluctance caused by slotting between stator and rotor.

A. The design strategy of Asymmetric PMASRM

At present, the most effective way to solve the torque ripple is to use asymmetric rotor structure, In order to solve this problem, a novel asymmetric flux barrier structure is proposed in this paper. The structure is shown in the Fig. 16. This structure can not only weaken the torque ripple obviously, but also retain the advantage of low harmonic component of no-load back EMF.

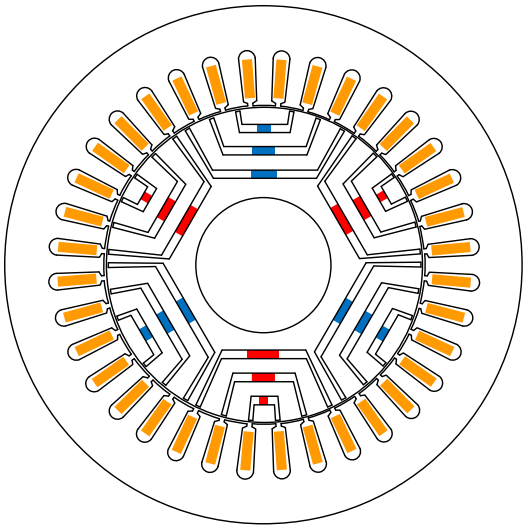

Fig. 16. FEA model of asymmetric PMASRM.

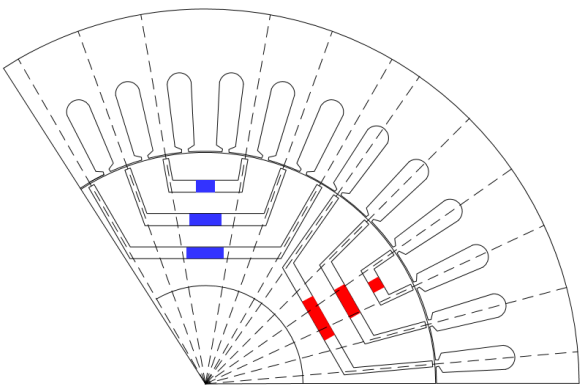

Fig. 17. Design of flux barriers of asymmetric PMASRM.

All the ends of flux barriers of N-pole are aligned with the teeth of the stator, and all the ends of flux

barriers of S-pole are aligned with the slots of the stator, as shown in the Fig. 17. When the motor rotates, half of the ends of the magnetic barrier aligns with the teeth, and the other half aligns with the slot. The rotor magnetic barriers are regarded as virtual slots and the rotor core as virtual teeth. By using this method, the cogging effect between stator and rotor can be weakened and the torque ripple can be further weakened.

The width of permanent magnet needs to be redefined due to the change of the original angle of magnetic barrier, i.e. the magnitude of α_1, α_2, α_3 and α_4. According to the method of optimizing the width of permanent magnets mentioned above, the widths of N-pole permanent magnets PM1N, PM2N and PM3N are 3.2mm, 5.4mm and 6.2mm, respectively; the widths of S-pole permanent magnets PM1S, PM2S and PM3S are 2 mm, 5.4mm and 7.4mm, respectively.

B. FEA of theasymmetric PMASRM

Similar to the Pre-optimized PMASRM, the FEA of Asymmetric PMASRM is carried out by Maxwell software. The air-gap flux density waveform and the harmonic content of Fourier analysis, no-load back EMF waveform, harmonic content, distortion rate and torque ripple under rated conditions are analyzed.

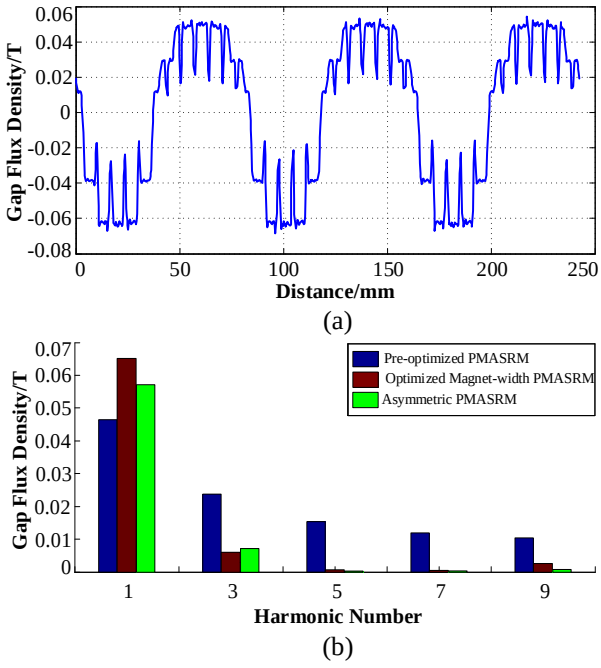

Fig. 18. (a) Air-gap flux density waveform of asymmetric PMASRM, and (b) harmonic analysis results of no-load back EMF for three kinds of motors.

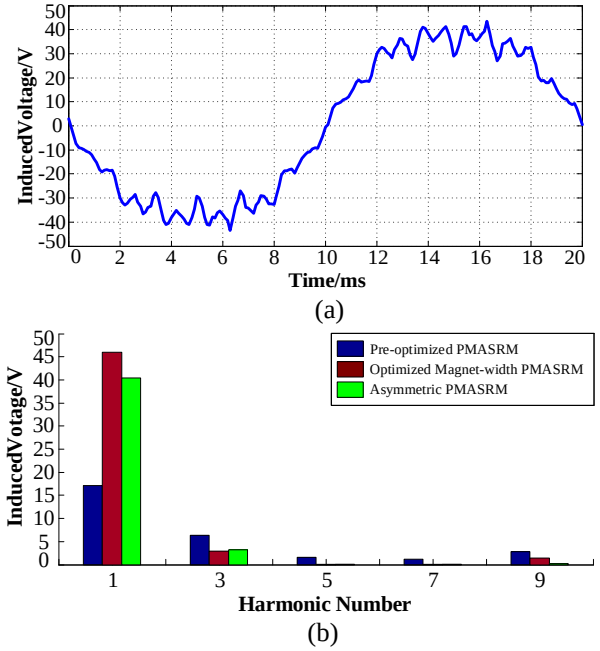

Fig. 19. (a) No-load back EMF waveform of asymmetric PMASRM, and (b) harmonic analysis results of no-load back EMF for three kinds of motors.

According to the analysis results in Fig. 18, it can be seen that the air-gap flux density waveform is asymmetrical because of the unsymmetrical magnetic barriers. The fundamental wave of the air-gap flux density waveform decreases and the harmonic component increases. The FFT and THD of no-load back EMF waveform are analyzed in Fig. 19. Although the fundamental wave decreases, the higher harmonic does not change significantly, and the THD of no-load back EMF waveform changes from 18.52% to 9.72%. Therefore, the Asymmetric PMASRM can further decrease the harmonic component of no-load back EMF, making it closer to the sinusoidal wave.

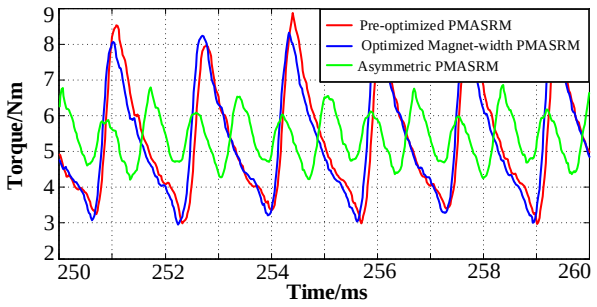

Fig. 20. Torque ripple for three kinds of motors.

As can be seen from Fig. 20, the torque ripple of Asymmetric PMASRM is further reduced compared with the former two motors, from 5.85Nm and 5.51Nm to 2.64Nm, which reduces the torque ripple significantly.

C. Motor efficiency at rated load

Efficiency is an important index of motor. Because the PMASRM exhibits high anisotropy, the harmonic content of stator and rotor flux density is serious [19]. Reducing the iron loss of motor is a key problem in optimizing the design of PMASRM. In this paper, the iron and copper losses of three kinds of structural motors in synchronous operation are obtained by FEA, and the results are present in Table 2 below.

Table 2: Efficiency of three kinds of motor under rated load

	Pre-Optimized PMASRM	Optimized Magnet-width PMASRM	Asymmetric PMASRM
Iron loss (W)	7.27	7.14	7.68
Copper loss (W)	69.10	66.79	64.46
Output power (W)	560	559.4	557.53
Efficiency	88%	88.32%	88.54%

From Table 2, it can be seen that the efficiency of the three kinds of structure motors is very similar, and all of them are above 88%, which fully meets the requirements of the design of PMASRM. It shows that the design of Asymmetric PMASRM with magnetic barrier is reasonable and feasible.

V. CONCLUSION

In this paper, a PMASRM with optimized permanent magnet width is proposed, and then an improved PMASRM with asymmetric magnetic barriers is proposed. The two-dimensional models of three kinds of PMASRM with different rotor structures are established and analyzed by FEA. The air-gap flux density waveforms, no-load back EMF waveforms and their harmonic analysis of the three kinds of motors are obtained, and the torque ripple under rated load is compared. The results show that the air-gap flux density waveform, induction electromotive force waveform and current waveform of Optimized Magnet-width PMASRM and Asymmetric PMASRM are closer to sinusoidal distribution than those of conventional PMASRM with the same amount of permanent magnet, and the torque ripple of Asymmetric PMASRM decreases significantly under the same load. It proves the rationality of optimizing the design of permanent magnet width motor and asymmetric magnetic barrier motor.

ACKNOWLEDGMENT

This work was supported by the Natural Science Foundation of Jiangsu Province Grant No. BK20190634.

REFERENCES

[1] M. De Gennaro, J. Jürgens, A. Zanon, J. Gragger, E. Schlemmer, A. Fricassè, L. Marengo, B. Ponick, E. T. Olabarri, J. Kinder, A. Cavallini, P. Mancinelli, M. Hernandez, and M. Messagie, "Designing, prototyping and testing of a ferrite permanent magnet assisted synchronous reluctance machine for hybrid and electric vehicles applications," *Sustainable Energy Technologies & Assessments*, vol. 31, pp. 86-101, Jan. 2019.

[2] J. X. Shen, "Analysis and design of synchronous reluctance machines PART I: An overview," *Microwaves*, vol. 44, no. 10, pp. 72-79, Oct. 2016.

[3] X. Liu, Y. Li, Z. Liu, T. Ling, and Z. Luo, "Optimized design of a high-power-density PM-assisted synchronous reluctance machine with ferrite magnets for electric vehicles," *Archives of Electrical Engineering*, vol. 66, no. 2, pp. 279-293, 2017.

[4] K. Wang, Z. Q. Zhu, G. Ombach, M. Koch, S. Zhang, and J. Xu, "Torque ripple reduction of synchronous reluctance machines: using asymmetric flux-barrier", *COMPEL - The International Journal for Computation and Mathematics in Electrical and Electronic Engineering*, vol. 34, no. 1, pp. 18-31, Jan. 2015.

[5] T. Mohanarajah, J. Rizk, A. Hellany, M. Nagrial and A. Klyavlin, "Torque ripple improvement in synchronous reluctance machines," *2018 2nd International Conference on Electrical Engineering (EECon)*, Colombo, pp. 44-50, Sept. 2018.

[6] M. Sanada, K. Hiramoto, S. Morimoto, and Y. Takeda, "Torque ripple improvement for synchronous reluctance motor using an asymmetric flux barrier arrangement," *38th IAS Annual Meeting on Conference Record of the Industry Applications Conference*, vol. 1, pp. 250-255, Oct. 2003.

[7] M. Davoli, C. Bianchini, A. Torreggiani, and F. Immovilli, "A design method to reduce pulsating torque in PM assisted synchronous reluctance machines with asymmetry of rotor barriers," *2016 42nd Annual Conference of the IEEE Industrial Electronics Society* (*IECON)*, pp. 1566-1571, Oct. 2016.

[8] M. Xu, G. Liu, and Q. Chen, "Torque ripple improvement for ferrite-assisted synchronous reluctance motor by using asymmetric flux-barrier arrangement," *International Journal of Applied Electromagnetics & Mechanics*, pp. 1-10, 2019.

[9] N. Bianchi, E. Fornasiero, and W. Soong, "Selection of PM flux linkage for maximum low-speed torque rating in a PM-assisted synchronous

reluctance machine," *IEEE Transactions on Industry Applications*, vol. 51, no. 5, pp. 3600-3608, 2015.
[10] N. Bianchi, S. Bolognani, D. Bon, and M. Dai Pre, "Rotor flux-barrier design for torque ripple reduction in synchronous reluctance and PM-assisted synchronous reluctance motors," *IEEE Transactions on Industry Applications*, vol. 45, no. 3, pp. 921-928, 2009.
[11] N. Bianchi, S. Bolognani, D. Bon, and M. Dai PrÉ, "Torque harmonic compensation in a synchronous reluctance motor," *IEEE Transactions on Energy Conversion*, vol. 23, no. 2, pp. 466-473, June 2008.
[12] H. Cai, B. Guan, and L. Xu, "Low-cost ferrite PM-assisted synchronous reluctance machine for electric vehicles," *IEEE Transactions on Industrial Electronics*, vol. 61, no. 10, pp. 5741-5748, Oct. 2014.
[13] F. Xing, W. Zhao, and B. Kwon, "Design of a novel rotor structure for PM-assisted synchronous reluctance machines to improve torque characteristics," *2016 IEEE Conference on Electromagnetic Field Computation (CEFC)*, Miami, FL, pp. 1-1, 2016.
[14] R. Rouhani, S. E. Abdollahi, and S. A. Gholamian, "Torque ripple reduction of a synchronous reluctance motor for electric vehicle applications," *2018 9th Annual Power Electronics, Drives Systems and Technologies Conference (PEDSTC)*, Tehran, pp. 386-391, 2018.
[15] B. Boazzo, A. Vagati, G. Pellegrino, E. Armando, and P. Guglielmi, "Multipolar ferrite-assisted synchronous reluctance machines: A general design approach," *IEEE Transactions on Industrial Electronics*, vol. 62, no. 2, pp. 832-845, Feb. 2015.
[16] X. Zhang, L. Zeng, and R. Pei, "Designing and comparison of permanent magnet synchronous reluctance motors and conventional motors in electric vehicles," *2018 21st International Conference on Electrical Machines and Systems (ICEMS)*, Jeju, pp. 202-205, 2018.
[17] R. T. Ugale and B. N. Chaudhari, "A new rotor structure for line start permanent magnet synchronous motor," *2013 International Electric Machines & Drives Conference*, Chicago, IL, pp. 1436-1442, 2013.
[18] H. Huang, Y. Hu, Y. Xiao, and H. Lyu, "Research of parameters and anti-demagnetization of rare-earth-less permanent magnet assisted synchronous reluctance motor," 2015 *IEEE International Magnetics Conference (INTERMAG)*, Beijing, pp. 1-1, 2015.
[19] N. Bianchi and M. Barcaro, "Iron losses reduction in synchronous motors with anisotropic rotor," *2008 34th Annual Conference of IEEE Industrial Electronics*, Orlando, FL, pp. 1258-1263, 2008.

Xianming Deng was born in Sichuan, China. He received his B.S., M.S., and Ph.D. in Electrical Engineering from China University of Mining and Technology, Jiangsu, China. He is currently a Professor in the School of Electrical and Power Engineering of China University of Mining and Technology. His current research fields include power electronics and motor drive.

Ran Li was born in Shanxi, China. He received his B.S. in Electrical Engineering from Shandong University of Technology, Shandong, China. He is currently receiving a Master education at China University of Mining and Technology. His current research interests include power electronics and motor drive.

Lei Hao was born in Shandong, China. He received his B.S. in Electrical Engineering from Shandong University of Technology, Shandong, China. He is currently receiving a Master education at China University of Mining and Technology. His current research interests include power electronics and motor drive.

Ankang Zhang was born in Jiangsu, China. He received his B.S. in Electrical Engineering and Intelligent Control from Nantong University, Jiangsu, China. He is currently receiving a Master education at China University of Mining and Technology. His current research interests include Motor control and transformer design.

Junhong Zhou was born in Hunan, China. He received his B.S. in Information Engineering from China University of Mining and Technology, Jiangsu, China. He is currently receiving a Master education at China University of Mining and Technology. His current research interests include power electronics and motor drive.